Automatic Segmentation of Macular Holes in Optical Coherence Tomography Images

ODILON L. C. MENDES[ID]**[1], DANIEL R. LUCENA**[ID]**[1], ABRAHÃO R. LUCENA**[ID]**[1],**
TARIQUE S. CAVALCANTE[ID]**[1],**
VICTOR HUGO C. DE ALBUQUERQUE[ID]**[2,3], (Senior Member, IEEE),**
METEB ALTAF[ID]**[4], MOHAMMAD MEHEDI HASSAN**[ID]**[5], (Senior Member, IEEE),**
AND AUZUIR R. ALEXANDRIA[ID]**[1]**

[1]Federal Institute of Education, Science and Technology of Ceará (IFCE), Fortaleza 60040-215, Brazil
[2]Graduate Program on Teleinformatics Engineering, Federal University of Ceará, Fortaleza 60455-970, Brazil
[3]Graduate Program on Telecommunication Engineering, Federal Institute of Education, Science and Technology of Ceará, Fortaleza 60040-531, Brazil
[4]Advanced Manufacturing and Industry 4.0 Center, King Abdulaziz City for Science and Technology, Riyadh 11442, Saudi Arabia
[5]Research Chair of Smart Technologies, Information Systems Department, College of Computer and Information Science, King Saud University, Riyadh 11543, Saudi Arabia

Corresponding author: Mohammad Mehedi Hassan (mmhassan@ksu.edu.sa)

ABSTRACT The retina is a part of the ocular system responsible for vision. In the central region of the retina is the macula, that enables detailed view. There is a distinct macular disease called Macular Hole (MH). It causes a condition of low vision related to the weakening of the fovea, high myopia, eye trauma and severe exposure to the sun. A surgery depends of the size and shape of the MH. A macular hole can be identified in Optical Coherence Tomography (OCT) images through the top boundaries of the Internal Limiting Membrane (ILM) and the Retinal Pigment Epithelium (RPE). Manual segmentation of OCT images is time consuming whereas automatic segmentation is fast and has a low computational cost, and consequently of interest to specialists. Thus, the main objective of this work is to develop an algorithm that automatically segments the ILM boundary layer and the area of the MH in OCT images. Another objective that was also pursued included the automatic acquisition of MH measurements. The segmentation was performed through a set of techniques involving shortest distance from a point to a curve (Euclidean Distance), Flood Fill and Border Following algorithms. The proposed method reached satisfactory results for all applications made. The automatic segmentation of MH and the extraction of its measures is a significant contribution to aid the medical diagnosis of the macular hole pathology.

INDEX TERMS Image processing, macular hole (MH), optical coherence tomography (OCT), segmentation.

I. INTRODUCTION

The retina is a part of the ocular system responsible for vision, and in its central region is the macula, that is responsible for sharp vision [1]. Among the various possible abnormal conditions of the macula, the macular hole (MH) is the less commonly encountered [2]. The incidence of this pathology relates to age, occurring usually in people over the age of 50 years and mostly in women [3]. Still, for people under 40 years, the MH can affect about 1 in 500 people [4].

The associate editor coordinating the review of this manuscript and approving it for publication was Kumaradevan Punithakumar[ID].

Macular hole is a condition of low vision related to the weakening of the fovea, high myopia, eye trauma and severe exposure to the sun, in which the rupture of the Internal Limiting Membrane (ILM) layer creates a hole in the retina [5]. Age is the most common cause of MH. With advancing age, the vitreous shrinks in size and separates from the retina. The problem is that sometimes it pulls the retina together, causing the macula to rupture. Eye damage or swelling of the macula due to other pathologies can also bring on the macular hole [6].

If a patient has a macula hole in only one eye, he/she will not usually complain until a significant decrease in vision

occurs. However, if the presence of the hole is bilateral, the complaints will come sooner. Among the symptoms commonly reported are loss of distant vision, difficulty in reading and gray spot in the central region of vision. Furthermore, some people report image distortion [7].

The MH format and measurements are necessary to determine the type of treatment. Some important metrics for the volume of the hole are areas, diameters and height. The measurement of these metrics are important to assess if it is possible to close the hole [8]–[10]. The identification of MH in Optical Coherence Tomography (OCT) images is possible through the top boundaries of the ILM and the Retinal Pigment Epithelium (RPE) [11]–[13].

OCT is the device most used as a way to map and determine the internal structure of the eye through images. This technique stands out for not causing any discomfort to the patient, as there is no physical contact [14]–[16]. This tool produces high quality retinal images. Although, it was first introduced in 1991 [17]–[19], it only appeared commercially in 1996 [20]. Now it is standard practice for medical retinal analysis [21]. Various A-scans (1D) build a B-scan (2D) image [22], and an aggregation of B-scans constructs a 3D structure [23]–[25].

Automatic segmentation and diagnosis of pathologies using OCT is not an easy task. More than one pathology in the same image may affect the results negatively. The same pathology may have different characteristics, and MH is one example. The guaranty of an identical comparison between regions is not possible in some studies using more than one dataset from different devices [26], [27].

The acquisition of information and the execution of tasks can be made through automatic techniques in images [28]. Countless preprocessing techniques can be applied for segmentation of images. Using medical images to make diagnoses has become both popular and reliable. Millions of images are produced by hospitals each year. These images have features that allow specialists to diagnose pathologies [29].

Although manual segmentation of OCT devices is carried out by specialists [30], this technique is time consuming which makes it disadvantageous for studies of segmentation and classification [31]–[35]. On the other hand, manual segmentation is still the major segmentation technique for OCT images due to the lack of reliable automated methods [36]. Thus, a fast and low computational cost segmentation technique would be of great interest to help specialists to analyze retinal layers. Furthermore, the advances in research involving this area can contribute to the acceptance of this technology in medical practices [37]. Therefore, The main objective of this work is the development of an algorithm that automatically segments the ILM boundary layer and the area of a MH pathology in OCT images.

The importance of understanding the clinical case and all its variables is fundamental for the development of this work. Health and technology are areas that complement each other. Health provides the necessary elements for the methodological basis of new technologies. While technology benefits health with improved and robust equipment and procedures that improve the quality of life for society as a whole.

II. RELATED WORKS

A limited number of works have been made in the field of automatic segmentation of MH in OCT images. Keller *et al.* [38] created an algorithm to segment the MH boundary layer. A comparison between the shortest path and length-adaptive segmentation techniques aims to prove that length-adaptive segmentation reaches better results. However, this work did not acquire the MH measures, which are important in the diagnosis decision.

Nasrulloh *et al.* [39] created a technique that allows the 3D segmentation of the macular hole through image cuts. Through this approach it was possible to acquire bi and three-dimensional measurements. A set of images of the same eye is needed to assemble the three-dimensional mosaic, forming the MH volume.

Xu *et al.* [40] suggested a method to segment the MH volume through the segmentation of two boundary layers, ILM and RPE. Through the graph cuts technique, for each frame there is an independent segmentation. The last two methods require a large amount of computational resources because the use of a large number of images. A simple methodology should be developed for automatic segmentation and extraction of measures of MH in OCT images.

III. METHODOLOGY

Medicine has evolved considerably with devices that allow the acquisition of increasingly clear digital images. However, inaccurate diagnosis can occur through the use of some medical images. Some factors can be responsible for it, such as the presence of noise or difference in the contrast in some parts of the image. Suitable algorithms for image processing are necessary in order to obtain better results. Two types of segmentation are implemented in this work: distance-based segmentation and area-based segmentation. A flowchart of the methodology is shown in Figure 1.

The proposed method is a set of techniques, including shortest distance from a point to a curve, Flood Fill and Border Following algorithms that work together. They are applied throughout the development of the proposed work.

The algorithm was implemented using Python language. The computer is equipped with Windows 10 platform with an Intel Core i7 CPU at 2.5 GHz and 8 GB RAM. The OCT images used in this work all came from a public source called Optical Coherence Tomography Image Retinal Database (OCTID) [41], [42]. The high-resolution JPEG images have 2 mm scan length and 500×750 pixel size (1 pixel ~ 3.9 μm). A Cirrus HD-OCT machine was used. The OCTID database contains more than 500 images classified in different conditions. For this work, only images with MH were necessary (102 B-scan OCT images).
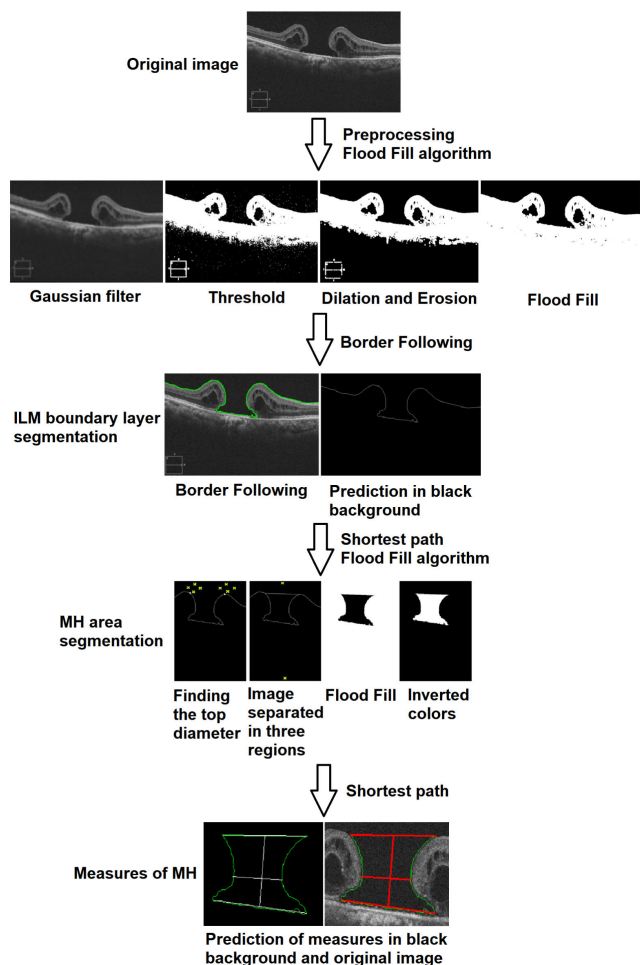
Original image

Preprocessing
Flood Fill algorithm

Gaussian filter   Threshold   Dilation and Erosion   Flood Fill

Border Following

ILM boundary layer segmentation

Border Following   Prediction in black background

Shortest path
Flood Fill algorithm

MH area segmentation

Finding the top diameter   Image separated in three regions   Flood Fill   Inverted colors

Shortest path

Measures of MH

Prediction of measures in black background and original image

FIGURE 1. Flowchart of the methodology.

A specialist from *Escola Cearense de Oftalmologia* (Fortaleza, Brazil) contributed to the work by creating the ground-truth (GT) of the ILM and MH area contours segmentations. In addition, MH measurements were also extracted for further evaluation. Images that were not a full-thickness MH were excluded by the specialist. Among the 37 discarded images were conditions related to macular edema, macular pseudo hole, lamellar macular hole, epiretinal membrane, vitreomacular traction syndrome and MH with retinal detachment. There were also normal macula images in the MH image dataset. A total of 65 MH images were used.

Only one public database was found in the academic community containing OCT images with the macular hole pathology. Although 67 OCT images appear to be a small amount of samples, they are sufficient to confirm the performance of the method, as machine learning techniques are not used and consequently there is no need to train and test the algorithm using a large number of images.

A. IMAGE PREPROCESSING

The purpose of preprocessing is to improve the image quality, correcting defects and highlighting important details for

the desired application. This step is important to provide satisfactory results in segmentation. Various preprocessing techniques can be used, such as: brightness and contrast adjustment, noise reduction, correction of irregular lighting, edge enhancement, among others [1], [43].

The database has images taken with different settings. Consequently, the images had varying levels of brightness, which hindered the development processes. Therefore, all images were adjusted to normalize brightness by taking the brightness of one image as a reference for the others. Considering the influence of the brightness level (BL) in the final segmentation through experiment with images of different brightness intensities, the image MH5 obtained the best performance (BL of 0.1336). So, this image was used as the reference. Therefore, the BL of 0.1336 was considered to be optimal and adjustment conditions were employed. For example, if an image has a BL of 0.25, its BL is multiplied by 0.65, so that it is within the optimum BL margin (0.11 < BL < 0.15) that can be seen in Table 1. If brightness level is between 0.11 and 0.15 no adjustment is necessary.

TABLE 1. Brightness level adjustment.

Brightness Level (BL)	Alpha
BL $\geq$ 0.23	0.65
0.15 $\leq$ BL < 0.23	0.85
0.11 < BL < 0.15	1.00
0.08 < BL $\leq$ 0.11	1.30
BL $\leq$ 0.08	1.60

It is important to understand that just the value 0.1336 is necessary, the image MH5 served only in the development of the methodology. It is not necessary to use any reference image whenever the algorithm runs.

A small area was used to measure the brightness level of the images. Its pixel location in any image is (10:50,350:390). An example of OCT image with this small area is shown in Figure 2. This area position was chosen because it is the vitreous body of the eye for all the images. This position does not contain any type of layer of the human eye. The images must be in the gray scale mode.

FIGURE 2. OCT image with an area marked in red to measure the brightness level.

OCT images have noise, especially Gaussian noise. Smoothing (blurring) techniques help reduce it. A Gaussian filter with a kernel size of pixel of 11×11 is used.

B. THRESHOLDING

In medical images, the separation of regions with the objects of interest from the background is an useful task. Thresholding is a good option for this. Since it performs segmentation based on pixel intensity [44]. The cutoff point of 45 is applied to all pixels, ranging from 0 to 255 in shades of gray. This cutoff was chosen as it best suits a good segmentation for a pattern of images processed following the applied methodology. A thresholding result is shown in Figure 3.
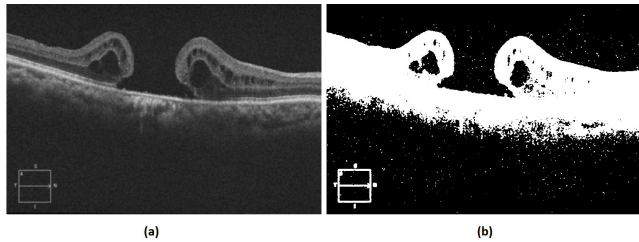

FIGURE 3. (a) Gaussian Blur filtered image and (b) thresholded image.

If the image used as a reference for brightness level normalization was a different one, perhaps another threshold value would be chosen. The alignment between the parameters of all applied techniques is necessary for the good performance of the algorithm.

C. MORPHOLOGICAL OPERATIONS

Examples of morphological operations used in this work are erosion and dilation. Removing pixels at the edge of objects is accomplished by erosion. Dilation does the inverse, it adds pixels. Some parameters must be set before starting the technique. They are the choice of the shape and size of the structuring element [45].

The kernel used in both dilation and erosion is 3×3. Two erosions and two dilations are applied alternately. This approach removes small white objects, preserving the contours of the boundaries that are essential to perform a satisfactory segmentation. After the series of two erosions and two dilations have been performed, the bottom half of the image becomes a black space, as can be seen in Figure 4(a).
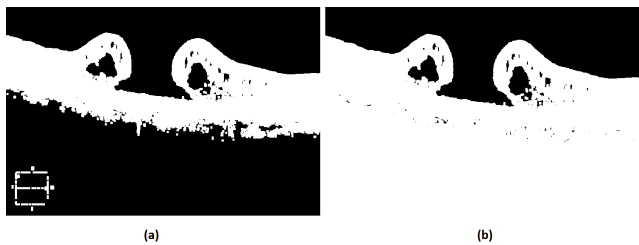

FIGURE 4. (a) A series of erosions and dilations and (b) Flood Fill application.

As it is essentially a work on image processing, the proposed methodology include morphological operations. These techniques have implications for a large number of initial

adjustments while moving from one data to other, but this is performed in the development of the algorithm. When everything is ready, it is no longer necessary to keep adjusting parameters, the methodology works automatically.

D. FLOOD FILL ALGORITHM

The Flood Fill algorithm is most commonly used to fill the holes in the given input image. For binary images, it changes the background pixels to foreground pixels until it reaches the object boundaries [46]. The Flood Fill algorithm is represented by:

$$src(x', y') - loD \leq src(x, y) \leq src(x', y') + upD, \quad (1)$$

where $src(x, y)$ is the coordinate value of the pixel under evaluation; $src(x', y')$ is the neighbor pixel connected component; loD and upD are the maximal lower and the maximal upper brightness differences between the observed pixel and its neighbors that are already connected component, or a seed pixel being added to the component, respectively. Summarizing, a Flood Fill algorithm may be divided into the following steps:

1) definition of the position of the starting point (seed point);
2) choice of the neighboring pixels method (kernel);
3) decision of a replacement color and a target color;
4) definition of the path and directions that will be taken by the seed point;
5) analyze each pixel found and define whether or not to replace its color;
6) repetition of step 5 until the algorithm has covered all the pixels within the boundaries.

The Flood Fill algorithm is the first step in the set of techniques applied. The chosen kernel or neighboring pixels uses the 8-connected method. This kernel includes the diagonal pixels. Hence, it would correctly fill any format. A specified seed point is chosen (550,470) and reassign all pixel values until reaches the object boundary. The chosen coordinates are at the position close to the bottom of the image because the objective of this step is to separate the image into two regions (black and white).

The objective is to make the bottom space white (Figure 4(b)). Thereby, the ILM boundary layer is well defined, separated by the forward and background regions, so that it can be segmented.

E. BORDER FOLLOWING ALGORITHM

After the Flood Fill application, the ILM boundary layer is differentiated, therefore being segmented. This segmentation step is performed by finding the largest contour between the white object and the background; this is done because the binary image has small black holes that also form small contours.

Then, the second step of the set of techniques is performed, that is the Border Following algorithm. It extract the topology of a binary image. This technique starts through the choice of
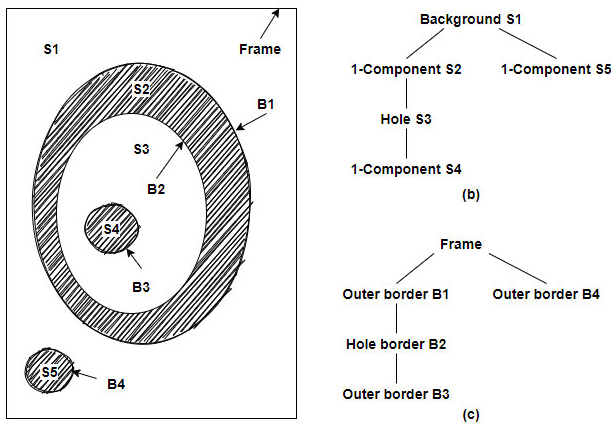
FIGURE 5. Border Following algorithm.

the starting point, which is usually the top left corner pixel in the image. When the algorithm finds a pixel (i, j) that satisfies an edge condition, a label is assigned to it. All pixels that are part of this identified border will receive the same label.

After completing the first scan, the next step is to look for edges within the borders already found. The algorithm does the same process, but in smaller search spaces delimited by the borders, which can form closed areas. Each pixel found with a border condition that is not part of the previous borders receives a different identification label. When the scan reaches the bottom right corner of the image, the algorithm stops. At the final of the process all borders will be obtained and have a unique identification label [47]. The Border following algorithm is shown in Figure 5. This technique allows to know the number of borders in an image and also it allows to choose the largest contour, for example.
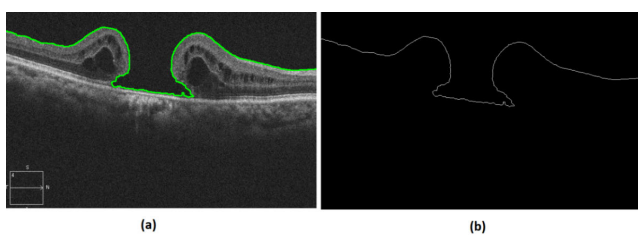

FIGURE 6. (a) ILM boundary layer segmentation on the original image, and (b) on the background.

Three components are necessary: the first is the source image, the binarized image after the Flood Fill algorithm; the second is the contour retrieval mode, the approach retrieves only the largest contour, and the side and bottom cuts in the image eliminate unwanted parts of the contour; the third is the contour approximation method, it compresses horizontal, vertical, and diagonal segments and leaves only their end points. The contour method generates an array of (x, y) coordinates from the largest contour related to the black background. The result is the ILM boundary layer segmentation that is represented in Figure 6.

F. SHORTEST DISTANCE FROM A POINT TO A CURVE

The segmentation of a MH area is obtained by applying the third step of the set of techniques. The extreme top left and top right pixels of the MH must be located. The shortest distance from a point to a curve (Euclidean Distance (ED)) is used to find these pixels. This technique will be explained based on the theory used to compare the prediction of an ILM boundary layer segmentation with its respective ground-truth. This same method is used to obtain the segmentation results and it is also used in the third step of the methodology to obtain specific pixels that are used to close the macular hole through the top diameter. The theory of shortest distance from a point to a curve is represented in Figure 7.
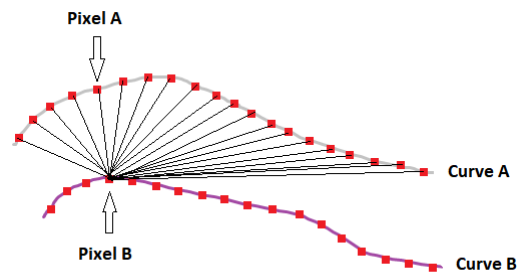

FIGURE 7. Shortest distance from a point to a curve.

For each pixel of the curve B (prediction), the ED calculation is performed with all pixels of curve A (ground-truth). Then, the shortest pixel of A will be chosen to calculate the distance error at that local pixel of B. The process is carried out from pixel to pixel of curve B with all pixels of curve A until all the pixels of curve B are performed. At the end of the process, there will be a shortest distance error for each pixel of B related to curve A. Then, the calculation of the main and standard deviation (SD) error between the two curves, prediction and GT, can be performed. In image analysis the space is two-dimensional and the Euclidean Distance is expressed by:

$$ED = \sqrt{(X_{seg} - X_{gt})^2 + (Y_{seg} - Y_{gt})^2}, \qquad (2)$$

where X_{seg} and X_{seg} are the coordinates of each pixel in the automatic segmented image, and X_{gt} and Y_{gt} are the coordinates of each pixel in the ground-truth image.

The objective of using ED is to find the shortest pixel of the curve related to each of two seed pixels fixed on the top left and top right at a certain distance from the center top of the image. These pixels will be the top left and top right points of a MH.

Four green cross marks are used to find each of the extreme pixels of the top diameter. The two pixels on the ILM contour that are shortest to the relationship between the four seed points will be the desired ones. The two sets of green cross marks (Figure 8(a)) were chosen empirically based on the pattern of MH contour in OCT images. They are located in the shortest region of the extreme pixels necessary to obtain the line that forms the top diameter. The two sets of green
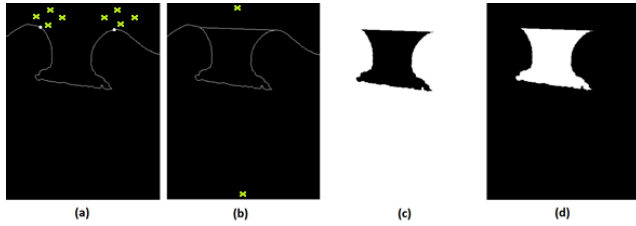
FIGURE 8. (a) Euclidean distance to find the shortest points (white) through the seeds (cross marks), (b) three regions and the seed points to apply the Flood Fill to, (c) MH area in black, (d) MH area after inversion of colors.

cross mark pixel locations are: ($Tpixel + 25,235$), ($Tpixel − 25,295$), ($Tpixel + 25,355$) and ($Tpixel + 75,285$) for the left set of pixels and ($Tpixel + 25,365$), ($Tpixel − 25,425$), ($Tpixel + 25,485$) and ($Tpixel + 75,435$) for the right set of pixels. Where *Tpixel* is the pixel of the ILM contour closest to the top of the image.

Having found these extreme pixels, the next step is to draw a straight line between them, closing the hole. Now with the closed area, the image can be separated into three regions, a bottom region, a top region and the one bounded by the macular hole. The Flood Fill technique is again applied to the upper and lower delimited regions of the image, leaving only the area of the macular hole in black. The seed points locations are (5,370) for the upper delimited region and (470,370) for the lower delimited region. Finally, the colors of the pixels are inverted, so the MH area becomes white and background becomes black. The process to obtain the MH area is summarized in Figure 8.

1) EVALUATION METRICS

In the case of the area-based segmentation, true positive (TP), true negative (TN), false positive (FP), and false negative (FN) are commonly used to classify pixels. A better understanding of this classification can be seen in the table 2 through a confusion matrix.

TABLE 2. Confusion matrix for MH area segmentation.

		Ground-truth	
		MH	Non-MH
Prediction	MH	TP	FP
	Non-MH	FN	TN

Some adopted evaluation metrics are: Accuracy, Intersection over Union (IoU) or Jaccard Index, Dice Similarity Coefficient (DSC) or F1 score and Matthews Correlation Coefficient (MCC). Accuracy simply calculates the percentage of pixels in the image correctly classified, but it can provide misleading results. There may be class imbalance, as TP and TN pixels can dominate the image. The amount of FP and FN pixels neglected can affect the reliability of the result [48]. Accuracy is defined by:

$$Accuracy = \frac{TP + TN}{TP + FP + TN + FN}. \quad (3)$$

In MCC, the higher the correlation between the predicted and GT values, the better the prediction. This metric is also perfectly symmetric, no class is more important than another. The MCC calculation is:

$$MCC = \frac{(TP \cdot TN) - (FP \cdot FN)}{\sqrt{(TP+FP) \cdot (TP+FN) \cdot (TN+FP) \cdot (TN+FN)}}. \quad (4)$$

The IoU and DSC are related to intersection of areas A (prediction) and B (GT). The IoU is the area of overlap between prediction and ground-truth divided by the area of union between them. The IoU calculation is described by:

$$IoU = \frac{A \cap B}{A + B - A \cap B}. \quad (5)$$

The DSC is similar to IoU. The area of overlap images is multiplied by 2 and divided by all the pixels in both images [48]. The DSC is expressed by:

$$DSC = \frac{2 \cdot (A \cap B)}{A + B}. \quad (6)$$

G. MEASUREMENTS OF THE MACULAR HOLE

Macular hole measurements are fundamental for the surgeon to decide whether or not a hole closure surgery is feasible. An important metric to decide a hole closure surgery is the Macular Hole Index (MHI). The MHI is the division between the height and the bottom diameter of a macular hole [49]. Patients are classified into two groups. If the MHI is greater than 0.5 the surgery can be performed without problems, however, if the MHI is less than 0.5 the possibility of closing the macular hole is less, so the surgery is less likely to be successful. The MHI is calculated based on the MH measurements:

$$MHI = \frac{height}{bottom diameter}. \quad (7)$$

Independent of the MHI, the most important measures for specialists at the time of analysis are: top diameter, bottom diameter, minimum diameter and height. To obtain these measures, some steps are necessary. The first step is to obtain the contour of the MH area. The Border Following algorithm that is applied to find the ILM boundary layer contour is also applied here.

Four seeds are used to find each of the extreme points of the MH area contour (top left, top right, bottom left and bottom right). The pixel on the MH area contour that is the shortest to the relationship between the four seed points will be the desired extreme point. These measurements of a shortest distance to a curve are calculated using the Euclidean Distance. Once again, the set of techniques is used. Figure 9 shows the sixteen seed points used to find the four extreme points of the MH area.

The four sets of pixel locations are: ($Tpixel + 25,235$), ($Tpixel − 25,295$), ($Tpixel + 25,355$) and ($Tpixel + 75,285$) for the top left set of pixels and ($Tpixel + 25,365$), ($Tpixel − 25,425$), ($Tpixel + 25,485$) and ($Tpixel + 75,435$) for the top right set of pixels, ($Bpixel,180$), ($Bpixel,300$),

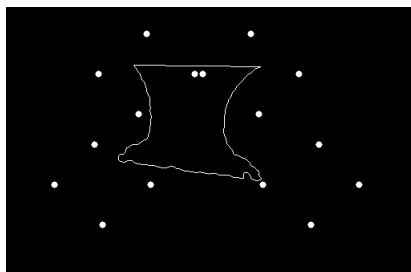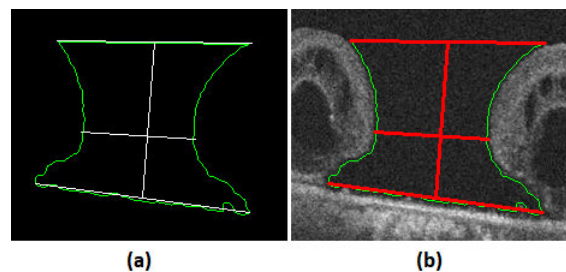**FIGURE 9.** Seed points used to find the extreme points of the MH area.

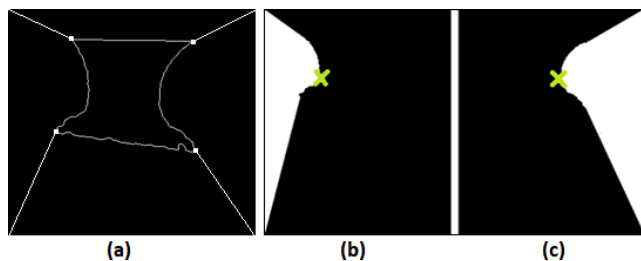**FIGURE 10.** Seed points of extreme areas in (b) and (c) to obtain the minimum diameter.

($Bpixel - 50,230$) and ($Bpixel + 50,240$) for the bottom left set of pixels and ($Bpixel,440$), ($Bpixel,560$), ($Bpixel + 50,500$) and ($Bpixel - 50,510$) for the bottom top right set of pixels. Where $Bpixel$ is the pixel of the MH area contour closest to the bottom of the image.

The top diameter is the distance between the top left and top right pixels of the MH area previously obtained. The bottom diameter is obtained in the same way as the top diameter, through the shortest distance using the ED method. The height is then determined using the midpoint of the bottom diameter and the midpoint of the top diameter and tracing a line between them.

The minimum diameter is obtained through the ED and Flood Fill algorithms. A straight line is drawn from the left pixel of the top diameter to the top left pixel of the image and another straight line is drawn from the left pixel of the base diameter to the bottom left pixel of the image, creating an area on the left side, which is filled through the Flood Fill. The most extreme right pixel in this area is the left pixel of the minimum diameter. The same process is carried out on the right side, finding the right pixel of the minimum diameter. Once the pixels are found, a line is drawn between them; this line is the minimum diameter. The process to find the minimum diameter is shown in Figure 10 and all the measures of a MH are represented in Figure 11.

The proposed methodology is a set of techniques that work together: shortest distance from a point to a curve, Flood Fill and Border Following algorithms. To facilitate the understanding of the work, the algorithm summarizing the methodology is divided into the following steps:

1) Load Libraries (cv2, numpy, imutils, skimage, math, matplotlib, warnings, imageio, PIL, sklearn, seaborn, pandas and time);

FIGURE 11. Measures of the MH in (a) background and (b) original image.

2) Analyze each image at a time ("for" loop);
3) Start counting time process;
4) Brightness adjustment normalization (Table 1);
5) Gaussian Blur filter to remove noise and enhance quality of image (kernel 11×11 pixel size);
6) Thresholding to binarize the image (cutoff point of 45);
7) Series of two erosions and two dilations alternately (kernel 3×3 pixel size);
8) Flood Fill algorithm at inferior background of image (seed at 550×470 coordinate and kernel using the 8-connected method);
9) Border Following algorithm to find the ILM boundary layer segmentation (contour retrieval mode chosen to get the longest contour; choice of contour approximation method; side and bottom cuts in the image to eliminate unwanted parts of the contour);
10) Compare prediction and ground-truth contours and get mean and standard deviation of distance error through the shortest distance from a point to a curve (Euclidean Distance);
11) Find the coordinates of the two top pixels of the curve to close the MH (shortest distance from a point to a curve);
12) Get MH area using Flood Fill algorithm at the inferior and superior areas of the image, isolating the macular hole;
13) Invert image colors to compare prediction and ground-truth through the confusion matrix of the pixels (evaluation metrics: accuracy, IoU, DSC and MCC);
14) Border Following algorithm to find MH area contour (same as step 9);
15) Get the six extreme points of the contour (shortest distance from a point to a curve and Flood Fill algorithm);
16) Evaluate the measurements of MH prediction through the comparison with the ground-truth measures.

IV. RESULTS AND DISCUSSIONS

The OCTID has 102 OCT images with MH, of which 65 were used. The 37 discarded images by the physician specialist contain examples of other conditions. Although these classes of holes are in the database, they do not fall within the scope of this study, as they are not interesting for physicians in terms of surgical analysis. Figure 12 shows some examples of the discarded images.
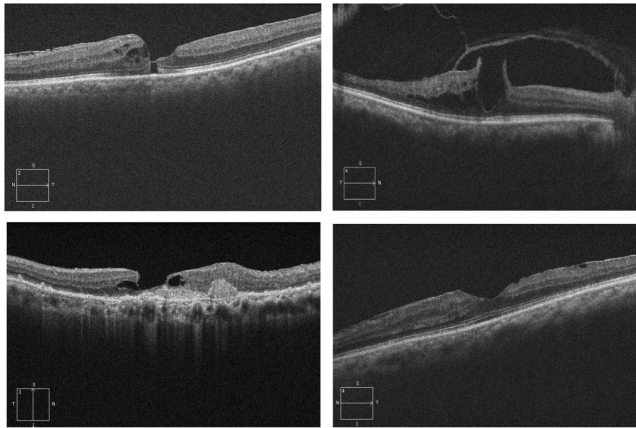
FIGURE 12. Examples of discarded images.

FIGURE 13. (a) Mean and (b) SD of unsigned error (pixel), and (c) MPT per image (s) of ILM boundary layer segmentation.

TABLE 3. Mean and SD of unsigned error comparison (pixel) and medium processing time per image (s) of ILM boundary layer segmentation.

Method	Mean and SD	MPT per image	Quant. images
Keller *et al.* (2016)	3.4 ± 5.74	2.65	50
Proposed method	2.72 ± 1.91	0.24	65

From left to right, top to bottom are examples of:

1) Macular pseudo hole, that is attributable to the centripetal contraction of an epiretinal membrane. ERM is always present in pseudo holes. It has the round and reddish appearance of a macula [50]. It is called a pseudo hole because the ILM and ERM layers do not touch each other, as in the case of a full-thickness MH.

2) Vitreomacular traction syndromeoccurs, that occurs because the posterior cortical vitreous begins to separate from the retina rapidly. Sometimes, the separation may be incomplete, resulting in persistent vitreous traction on the posterior retina [51].

3) Lamelar macular hole, that results from an interrupted formation of MH or may be a complication of a chronic macular cystoid edema [50]. As in the case of macular pseudo hole, the ILM and RPE layers do not touch each other, as in the case of a full-thickness MH.

4) Normal macula, where all layers are healthy. There is no presence of pathologies.

A. RESULTS FOR ILM BOUNDARY LAYER SEGMENTATION

The segmentation of the ILM boundary layer is part of the first step of the algorithm. A good segmentation of the MH area is only possible if this previous step has satisfactory results. As already mentioned, this step is part of the distance-based segmentation. The distance error of the shortest points to the curve has to be calculated by applying the Euclidean Distance. The evaluation metrics used are mean and standard deviation (SD) of the unsigned error (UE), and the medium processing time (MPT) per image. Boxplots with results are shown in Figure 13. The boxplot is important because it shows the median, the 50 % of the most likely values, and where the extreme values are located. It shows whether the algorithm is working in a standard way for all OCT images.

Outliers are the individual points distant from the median box. The few outliers in the boxplots may have been due to some points outside the curve that were not completely eliminated by the preprocessing techniques.
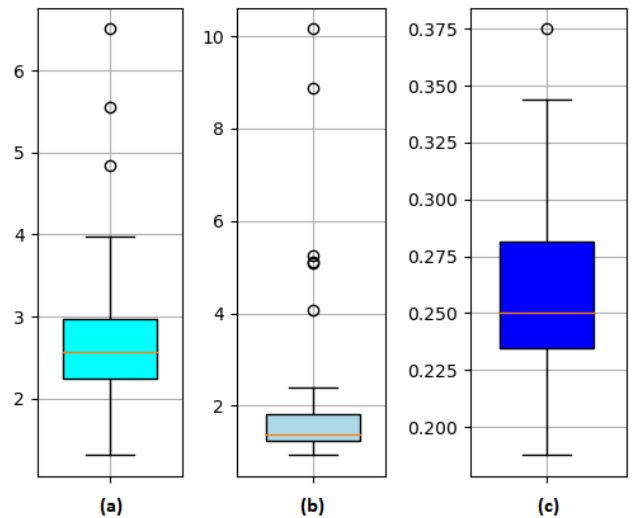
The proposed work is compared with a state-of-the-art method in order to validate and prove its effectiveness. A comparison of mean and standard deviation of unsigned error in pixels for the two methods is described in Table 3, as well the comparison between the MPT per image and the number of images used for both methods. Keller *et al.* [38] used a private database, while the proposed method used a public one. However, the images are similar and have the same characteristics, and thus do not affect the veracity of the comparison. The OCT images for both database were acquired using spectral domain optical coherence tomography (SD-OCT) technology. Furthermore, the images have the same pixel resolution (1 pixel $\sim$ 3.9 μm axially).

Keller *et al.* [38] is the only one of the three related works that evaluates the segmentation results of the ILM boundary layer. The other two approaches focus on area segmentation.

The mean and SD errors of distance between each pixel location of the ground-truth and the prediction contours segmentation were performed for both methods. The mean and SD of unsigned error were better in the proposed method. In the state-of-the-art method, the SD was greater than the mean; possibly this was because the algorithm confused objects outside the contour, and these objects appear due to a failure in the noise removal techniques. This was one of the difficulties found during the development of the proposed algorithm and motivated us to spend more time processing images before the segmentation.

The proposed method had a MPT per image of 0.24s (minimum and maximum processing time per image, respectively:

0.17s and 0.37s). The number of pixels that go through the mathematical operation of finding the shortest point to a curve can influence the variation in the processing time per image. That is, the longer the contour, the longer the processing time.

Although the proposed method uses more preprocessing techniques than the state-of-the-art method being compared, the processing time is shorter. Moreover, the computer used by Keller *et al.* [38] (Intel Core i7-4930K 3.4 GHz CPU) has a slight processing advantage over the one used in this work.

Another advantage of the proposed work is that MH measurements were made. Keller *et al.* [38] mentioned that the data obtained could be used to estimate measurements of MH. However, they did not perform any such calculations.

Therefore, the proposed work has significant importance to the scientific community in ILM boundary layer segmentation of OCT images with MH pathology due to the satisfactory results. These results are better than the state-of-the-art method with which it was compared. In addition, in the literature, as far as the author know, there is only one work based in ILM segmentation of OCT images that is directly focused on MH pathology.

B. RESULTS FOR MH AREA SEGMENTATION

Macular hole area segmentation is important as it can provide the shape and the measures of the hole. The different features in the shapes can be used in other applications, such as classification algorithms. Some of these features are the measures of diameters and height.

The MH area segmentation is only possible after a correct ILM boundary layer segmentation. This type of segmentation reinforces the effectiveness of the algorithm, since other evaluation metrics, such as accuracy, IoU, DSC and MCC can be applied.

The qualitative information given by the confusion matrix is another way to observe how well the algorithm is working. The confusion matrix for these related and unrelated areas is represented in Figure 14. The evaluation is performed by analyzing pixel by pixel of the predicted and ground truth MH areas.
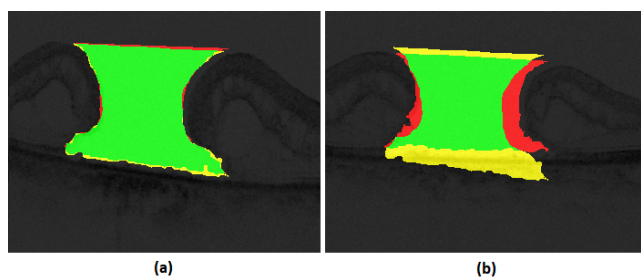

FIGURE 14. Confusion matrix of MH area segmentation for (a) related areas and (b) unrelated areas.

The green color (*TP*) occurs when the automatic area segmentation is correctly predicted. The red color (*FP*) occurs when the automatic area segmentation is incorrectly predicted. The shades of gray (*TN*) occur when the background
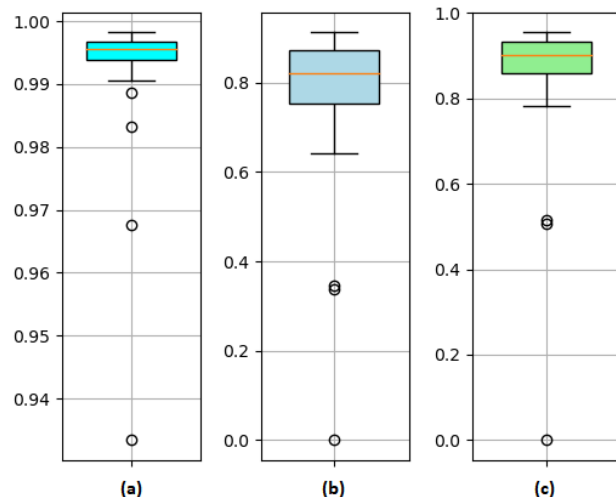

FIGURE 15. (a) accuracy, (b) IoU, and (c) DSC (%) for the evaluation of MH area segmentation.
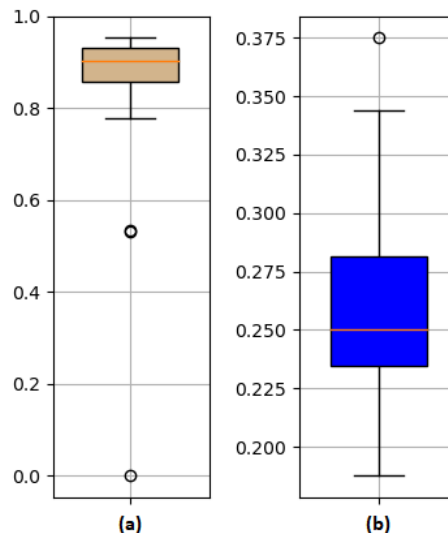

FIGURE 16. (a) MCC (%), and (b) MPT per image (s) for the evaluation of MH area segmentation.

is correctly predicted. The yellow color (*FN*) occurs when the GT is incorrectly predicted. Boxplots with the results of the evaluated metrics for all MH images are shown in Figure 15 and Figure 16.

There are few outliers, and they are acceptable, since the algorithm deals with various formats of area. These variations can generate more discrepancies in some results. Overall, the results are satisfactory.

There is an image with zero in the evaluation for IoU, DSC and MCC, which means that the algorithm was probably unable to segment the MH area for that image. Even so, the lowest accuracy value, which is probably of the image with failed area segmentation, has a value of 0.925. This high value explains why accuracy is not a robust form of

assessment for segmenting areas of images. The large amount of *TN* disguise the fact that the algorithm did not perform well. Therefore, for comparison accuracy was not taken into account.

Despite performing 3D segmentation, Nasrulloh *et al.* [39] is the only one of the three related works that evaluates the results of MH area segmentation in 2D images using the same metrics as the proposed method. This work approach a volumetric segmentation, requiring a larger number of images. These images must be of the same retina in order to form the volumetric segmentation. This is a favorable factor, since all images contain the same settings. However, there is no public database providing images of this type, especially for MH pathology.

Therefore, a comparison between this method and the proposed one requires some clarification. First of all the comparison is possible because to perform a volumetric segmentation it is necessary to perform several segmentations of area and then join them. However, the number of images is considerably greater for volumetric segmentations. The proposed work used only a public database that does not contain a large number of images. Thus, the processing time cannot be compared.

Although the databases are different the images are similar and have the same characteristics, which does not affect the veracity of the comparison. A comparison of IoU, and DSC for the methods is described in Table 4. The MCC metric was used for the proposed method, however, it was not used for the one being compared.

TABLE 4. IoU, DSC and MCC comparison (%) of MH area segmentation.

Method	IoU	DSC	MCC
Nasrulloh *et al.* (2017)	76.34 ± 10.31	86.19 ± 7.55	-
Proposed method	78.61	86.98	87

The methods achieved equivalent results. The MCC method, despite being considered one of the most appropriate and fair metrics to evaluate the effectiveness of an area segmentation algorithm, was not used by the compared state-of-the-art method. The MPT per image in the proposed method was of 19.95s (minimum and maximum processing time per image, respectively: 12.7s and 45.5s). The size of the MH area can influence the variation in processing time per image.

C. RESULTS FOR MEASUREMENTS OF MACULAR HOLES

Macular hole measurements are of fundamental importance for the specialists. These professionals need to take these measurements manually to calculate the possibilities of surgery. Automatic methods for that approach have been little explored by the scientific community. Despite the objective of this work was the contour and area segmentation of MH, an extension of the algorithm was performed in order to obtain these measurements. The mean and SD of unsigned error in micrometers for each measure prediction compared to the GT is shown in Table 5.

TABLE 5. Mean and SD of unsigned error (μm) for measurements of MH.

	Top diameter	Bottom diameter	Height	Minimum diameter
Proposed method	95.2 ± 79.2	106.8 ± 83.2	44.6 ± 55.4	41.9 ± 83

TABLE 6. Evaluation metric results for MHI classification in percentage.

	Accuracy	IoU
Proposed method	87.69	92.98

The comparison between studies regarding macular hole measurements was not possible, as only Nasrulloh *et al.* [39] performs these measurements, however using a different form from the proposed method to evaluate the results. Despite the work of Xu *et al.* [40] be directly related to the proposed work, its results evaluation techniques are only focused on 3D segmentation. It is not possible to make any comparison with the proposed methodology.

The Bland-Altman method was used to calculate the mean and SD of the unsigned errors in micrometers for each measurement. There are three horizontal lines in the graph, the center line is the mean error, and the other two are the maximum deviations given as references. The Bland-Altman graphs for the MH measurement errors are shown in Figure 17 to Figure 20.
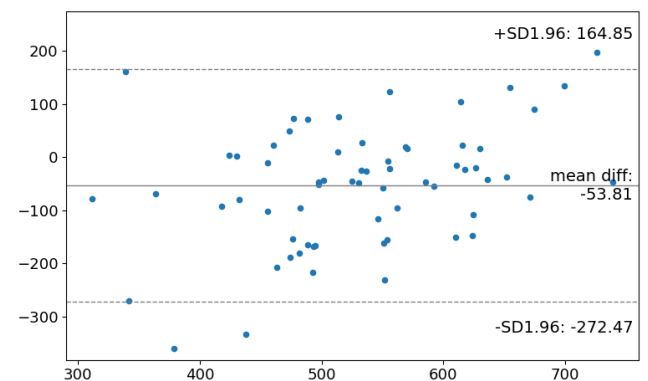

FIGURE 17. Mean and SD of signed error of MH top diameter (μm).

In order to generate a classification result by comparing the MHI of the GT measures and the MHI of the predictive measures, values of MHI above 0.5 receive the number 1, which will identify the possibility to perform a hole closure surgery, otherwise, the value 0 will be assigned, informing that surgery is not possible.

The confusion matrix in Figure 21 shows where the algorithm went right and wrong more clearly. Knowing the trend of the results of the proposed method is important. In order to evaluate the MHI, two metrics are used: accuracy and IoU. Table 6 shows the evaluation metric results.

The results for the mean and SD of signed error for the MH measurements show satisfactory values. This proves
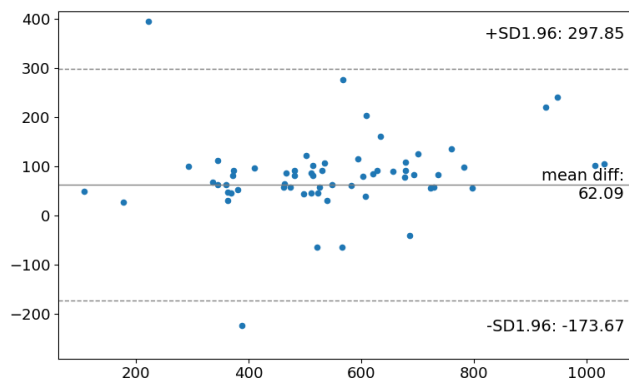
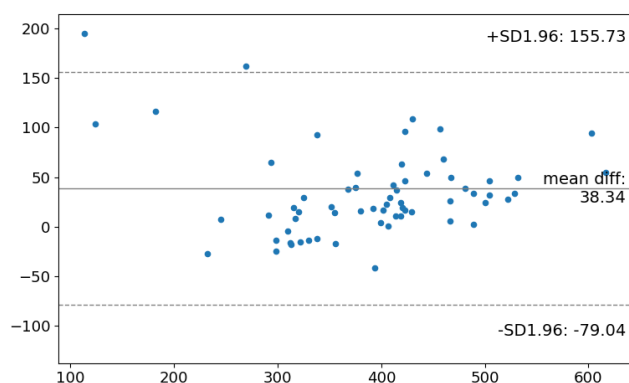**FIGURE 18.** Mean and SD of signed error of MH bottom diameter (μm).

FIGURE 19. Mean and SD of signed error of MH height (μm).
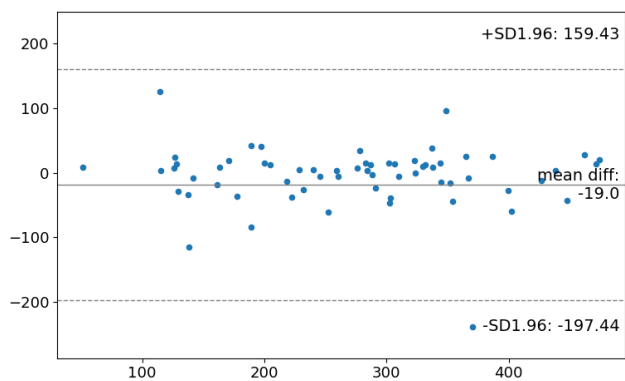

FIGURE 20. Mean and SD of signed error of MH minimum diameter (μm).

that in addition to performing two types of segmentation, the algorithm is also able to take measurements effectively. No measurement mean error was greater than 107 μm. The coherence of the results for the Bland-Altman graphics is also a good tool to analyze the capacity of the algorithm to stay within the standards results for all images.

Another important parameter is the Macular Hole Index. The results were satisfactory and showed that the algorithm can also be evaluated through an equation that relates the ability of the algorithm to perform a simple classification,
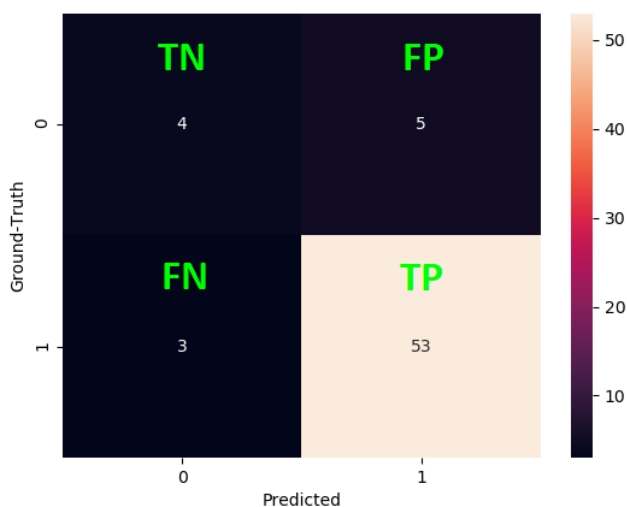

FIGURE 21. Confusion matrix of MHI.

without the need for more robust techniques, such as machine learning applications.

D. LIMITATIONS OF THE PROPOSED METHOD
The results of the proposed work were satisfactory, reaching both the main and specific objectives defined in the introduction through the validation techniques adopted. However, there are also some limitations. As an example, in image MH 14, the algorithm was unable to complete the MH area segmentation, which compromised the measurements. The area segmentation error of image MH 14 can be seen in Figure 22, where the pixels with color yellow are the *FN*, and the pixels with color red (almost imperceptible) are the *FP*.
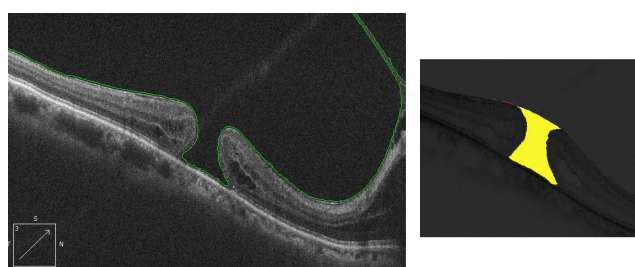

FIGURE 22. Contour segmentation (left) and confusion matrix of pixels (right) show a discrepancy between the prediction (red) and ground-truth (yellow).

The explanation for the error is that the contour of the ILM boundary layer is quite curved making the execution of the shortest distance from a point to a curve (trying to find the two points at the top of the image to close the area) to find points not consistent with the closing of the MH.

It is important to mention that the results of the automatic segmentation depend on the comparison with the ground-truth. In this work, only a single specialist performed the manual segmentations. The use of more than one specialist,

considering there are variances even among them, is relevant to reinforce the accuracy of the proposed methodology.

V. CONCLUSION

The main objective of this work, which is the development of an algorithm that automatically segmented the ILM boundary layer and the area of the MH pathology in OCT images, was reached. In addition, another objective was also achieved: the automatic acquisition of MH measurements.

The differential of the proposed work are: the set of techniques, the mathematical simplicity involved, and the ease of application. The proposed model is capable of performing the same function as a more complex technique, a machine learning method for example, with lower computational cost. The shortest distance from a point to a curve, Flood Fill and Border Following algorithms used in this work are consolidated tools, which can be implemented in any programming language.

The segmentation of an ILM boundary layer with a MH pathology is part of the first step of the algorithm. The proposed work was compared with a state-of-the-art method in order to validate and prove its effectiveness. The proposed method reached better results. For macular hole area segmentation the proposed method and the compared one achieved equivalent results.

The algorithm also obtained the measurements of MH. The results were satisfactory, thus proving that in addition to performing two types of segmentation the algorithm is also capable of taking measurements effectively.

The main contribution of this work is the importance of an automatic method to segment MH contour and area in OCT images and help the specialists. Furthermore, advances in research involving this area can contribute to the acceptance of automatic techniques in medical practices. This work may be a study source for researchers, clinicians and engineers wishing to delve into segmentation techniques.

Future prospects that will encourage the use of MH segmentation systems as proposed here in daily medical practices, are: the development of a classification algorithm with classes of MH and normal macula; the creation of a publicly database of OCT images with MH pathology containing ILM contour and MH area ground-truths; the use of more than a single specialist for the manual segmentation to reinforce the accuracy of the automatic segmentation; the design of an algorithm having the capability of discarding automatically abnormalities or data which are not related to MH pathology; the application of an embedded system in a mobile device; and the application of the approach to slices of B-scan images from the same MH, allowing 3D segmentation representation.

REFERENCES

[1] B. Hassan, G. Raja, T. Hassan, and M. U. Akram, "Structure tensor based automated detection of macular edema and central serous retinopathy using optical coherence tomography images," *J. Opt. Soc. Amer. A, Opt. Image Sci.*, vol. 33, no. 4, pp. 455–463, 2016.

[2] L. Zhang, W. Zhu, F. Shi, H. Chen, and X. Chen, "Automated segmentation of intraretinal cystoid macular edema for retinal 3D OCT images with macular hole," in *Proc. IEEE 12th Int. Symp. Biomed. Imag. (ISBI)*, Apr. 2015, pp. 1494–1497.

[3] T. L. Jackson, P. H. J. Donachie, J. M. Sparrow, and R. L. Johnston, "United Kingdom national ophthalmology database study of vitreoretinal surgery: Report 2, macular hole," *Ophthalmology*, vol. 120, no. 3, pp. 629–634, Mar. 2013.

[4] S. S. Thapa, R. Thapa, I. Paudyal, S. Khanal, J. Aujla, G. Paudyal, and G. V. Rens, "Prevalence and pattern of vitreo-retinal diseases in nepal: The Bhaktapur glaucoma study," *BMC Ophthalmol.*, vol. 13, no. 1, p. 9, Dec. 2013.

[5] H. Faghihi, F. Ghassemi, K. G. Falavarjani, G. S. Anari, M. Safizadeh, and K. Shahraki, "Spontaneous closure of traumatic macular holes," *Can. J. Ophthalmol.*, vol. 49, no. 4, pp. 395–398, Aug. 2014.

[6] American Academy of Ophthalmology. (2019). *What is a Macular Hole? What Causes a Macular Hole?* Accessed: Jun. 26, 2020. [Online]. Available: https://www.aao.org/eye-health/diseases/what-is-macular-hole

[7] Instituto de Retina. (2020). *Buraco Macular*. Accessed: Jun. 10, 2020. [Online]. Available: https://www.institutoderetina.com.br/home/

[8] J. Chhablani, M. Khodani, A. Hussein, S. Bondalapati, H. B. Rao, R. Narayanan, and A. Sudhalkar, "Role of macular hole angle in macular hole closure," *Brit. J. Ophthalmol.*, vol. 99, no. 12, pp. 1634–1638, Dec. 2015.

[9] D. Steel, H. Madi, and I. Masri, "Optimal management of idiopathic macular holes," *Clin. Ophthalmol.*, vol. 10, p. 97, Jan. 2016.

[10] D. H. W. Steel, C. Parkes, V. T. Papastavrou, P. J. Avery, I. A. El-Ghrably, M. S. Habib, M. T. Sandinha, J. Smith, K. P. Stannard, D. Vaideanu-Collins, and R. J. Hillier, "Predicting macular hole closure with ocriplasmin based on spectral domain optical coherence tomography," *Eye*, vol. 30, no. 5, p. 740, 2016.

[11] E. Philippakis, M. Legrand, M. El Sanharawi, A. Erginay, A. Couturier, and R. Tadayoni, "Measurement of full-thickness macular hole size using en face optical coherence tomography," *Eye*, vol. 32, no. 3, p. 590, 2018.

[12] T. Fabritius, S. Makita, M. Miura, R. Myllylä, and Y. Yasuno, "Automated segmentation of the macula by optical coherence tomography," *Opt. Exp.*, vol. 17, no. 18, pp. 15659–15669, 2009.

[13] J. D. Moura, J. Novo, S. Penas, M. Ortega, J. Silva, and A. M. Mendonça, "Automatic characterization of the serous retinal detachment associated with the subretinal fluid presence in optical coherence tomography images," *Procedia Comput. Sci.*, vol. 126, pp. 244–253, Jan. 2018.

[14] X. Sui, Y. Zheng, B. Wei, H. Bi, J. Wu, X. Pan, Y. Yin, and S. Zhang, "Choroid segmentation from optical coherence tomography with graph-edge weights learned from deep convolutional neural networks," *Neurocomputing*, vol. 237, pp. 332–341, May 2017.

[15] G. Gong, H. Zhang, and M. Yao, "Speckle noise reduction algorithm with total variation regularization in optical coherence tomography," *Opt. Exp.*, vol. 23, no. 19, pp. 24699–24712, 2015.

[16] C. Tang, X. Zheng, and L. Cao, "OCT despeckling via weighted nuclear norm constrained non-local low-rank representation," *Laser Phys. Lett.*, vol. 14, no. 10, Oct. 2017, Art. no. 106001.

[17] D. Huang, E. A. Swanson, C. P. Lin, J. S. Schuman, W. G. Stinson, W. Chang, M. R. Hee, T. Flotte, K. Gregory, and C. A. Puliafito, "Optical coherence tomography," *Science*, vol. 254, no. 5035, pp. 1178–1181, 1991.

[18] G. Coscas, J. Cunha-Vaz, and G. Soubrane, "Macular edema: Definition and basic concepts," in *Macular Edema*, vol. 47. Basel, Switzerland: Karger Publishers, 2010, pp. 1–9.

[19] P. G. Tranos, S. S. Wickremasinghe, N. T. Stangos, F. Topouzis, I. Tsinopoulos, and C. E. Pavesio, "Macular edema," *Surv. Ophthalmol.*, vol. 49, no. 5, pp. 470–490, 2004.

[20] J. S. Schuman, T. Pedut-Kloizman, E. Hertzmark, M. R. Hee, J. R. Wilkins, J. G. Coker, C. A. Puliafito, J. G. Fujimoto, and E. A. Swanson, "Reproducibility of nerve fiber layer thickness measurements using optical coherence tomography," *Ophthalmology*, vol. 103, no. 11, pp. 1889–1898, 1996.

[21] J. S. Schuman, *Optical Coherence Tomography of Ocular Diseases*, C. A. Puliafito, J. G. Fujimoto, and J. S. Duker. Eds. Thorofare, NJ, USA: Slack, 2004.

[22] W. Drexler, H. Sattmann, B. Hermann, T. H. Ko, M. Stur, A. Unterhuber, C. Scholda, O. Findl, M. Wirtitsch, J. G. Fujimoto, and A. F. Fercher, "Enhanced visualization of macular pathology with the use of ultrahigh-resolution optical coherence tomography," *Arch. Ophthalmol.*, vol. 121, no. 5, pp. 695–706, 2003.

[23] S. Ricco, M. Chen, H. Ishikawa, G. Wollstein, and J. Schuman, "Correcting motion artifacts in retinal spectral domain optical coherence tomography via image registration," in *Proc. Int. Conf. Med. Image Comput. Comput.-Assist. Intervent.* Berlin, Germany: Springer, 2009, pp. 100–107.

[24] J. Xu, H. Ishikawa, G. Wollstein, and J. S. Schuman, "3D OCT eye movement correction based on particle filtering," in *Proc. Annu. Int. Conf. IEEE Eng. Med. Biol.*, Aug. 2010, pp. 53–56.

[25] J. Hu, Y. Chen, and Z. Yi, "Automated segmentation of macular edema in OCT using deep neural networks," *Med. Image Anal.*, vol. 55, pp. 216–227, Jul. 2019.

[26] J. Ho, A. C. Sull, L. N. Vuong, Y. Chen, J. Liu, J. G. Fujimoto, J. S. Schuman, and J. S. Duker, "Assessment of artifacts and reproducibility across spectral- and time-domain optical coherence tomography devices," *Ophthalmology*, vol. 116, no. 10, pp. 1960–1970, Oct. 2009.

[27] G. Mylonas, C. Ahlers, P. Malamos, I. Golbaz, G. Deak, C. Schuetze, S. Sacu, and U. Schmidt-Erfurth, "Comparison of retinal thickness measurements and segmentation performance of four different spectral and time domain OCT devices in neovascular age-related macular degeneration," *Brit. J. Ophthalmol.*, vol. 93, no. 11, pp. 1453–1460, Nov. 2009.

[28] O. L. C. Mendes and G. M. R. Borille, "Computer vision systems in unmanned aerial vehicle: A review," *J. Mechtron. Eng.*, vol. 2, no. 2, pp. 11–22, Jul. 2019.

[29] N. Ayache, "Medical computer vision, virtual reality and robotics," *Image Vis. Comput.*, vol. 13, no. 4, pp. 295–313, 1995.

[30] M. Salarian, R. Ansari, J. Wanek, and M. Shahidi, "Acuurate segmentation of retina nerve fiber layer in OCT images," in *Proc. IEEE Int. Conf. Electro/Inf. Technol. (EIT)*, May 2015, pp. 653–656.

[31] K. Hu, B. Shen, Y. Zhang, C. Cao, F. Xiao, and X. Gao, "Automatic segmentation of retinal layer boundaries in OCT images using multi-scale convolutional neural network and graph search," *Neurocomputing*, vol. 365, pp. 302–313, Nov. 2019.

[32] G. N. Girish, A. R. Kothari, and J. Rajan, "Automated segmentation of intra-retinal cysts from optical coherence tomography scans using marker controlled watershed transform," in *Proc. 38th Annu. Int. Conf. IEEE Eng. Med. Biol. Soc. (EMBC)*, Aug. 2016, pp. 1292–1295.

[33] C. Wang, Y. X. Wang, and Y. Li, "Automatic choroidal layer segmentation using Markov random field and level set method," *IEEE J. Biomed. Health Informat.*, vol. 21, no. 6, pp. 1694–1702, Nov. 2017.

[34] D. C. Fernández, H. M. Salinas, and C. A. Puliafito, "Automated detection of retinal layer structures on optical coherence tomography images," *Opt. Exp.*, vol. 13, no. 25, pp. 10200–10216, 2005.

[35] K. A. Vermeer, J. Van der Schoot, H. G. Lemij, and J. F. De Boer, "Automated segmentation by pixel classification of retinal layers in ophthalmic OCT images," *Biomed. Opt. Exp.*, vol. 2, no. 6, pp. 1743–1756, 2011.

[36] N. George and C. V. Jiji, "Two stage contour evolution for automatic segmentation of choroid and cornea in OCT images," *Biocybern. Biomed. Eng.*, vol. 39, no. 3, pp. 686–696, Jul. 2019.

[37] O. L. C. Mendes, A. R. Lucena, D. R. Lucena, T. S. Cavalcante, and A. R. D. Alexandria, "Automatic segmentation of macular holes in optical coherence tomography images: A review," *J. Artif. Intell. Syst.*, vol. 1, no. 1, pp. 163–185, 2020.

[38] B. Keller, D. Cunefare, D. S. Grewal, T. H. Mahmoud, J. A. Izatt, and S. Farsiu, "Length-adaptive graph search for automatic segmentation of pathological features in optical coherence tomography images," *J. Biomed. Opt.*, vol. 21, no. 7, Jul. 2016, Art. no. 076015.

[39] A. V. Nasrulloh, C. G. Willcocks, P. T. G. Jackson, C. Geenen, M. S. Habib, D. H. W. Steel, and B. Obara, "Multi-scale segmentation and surface fitting for measuring 3-D macular holes," *IEEE Trans. Med. Imag.*, vol. 37, no. 2, pp. 580–589, Feb. 2018.

[40] D. Xu, A. Yuan, P. K. Kaiser, S. K. Srivastava, R. P. Singh, J. E. Sears, D. F. Martin, and J. P. Ehlers, "A novel segmentation algorithm for volumetric analysis of macular hole boundaries identified with optical coherence tomography," *Investigative Opthalmol. Vis. Sci.*, vol. 54, no. 1, p. 163, Jan. 2013.

[41] P. Gholami, P. Roy, M. K. Parthasarathy, and V. Lakshminarayanan, "OCTID: Optical coherence tomography image database," *Comput. Electr. Eng.*, vol. 81, Jan. 2020, Art. no. 106532.

[42] OCTID. (2018). *Optical Coherence Tomography Image Database Scholars Portal Dataverse*. Accessed: Oct. 25, 2019. [Online]. Available: https://dataverse.scholarsportal.info/dataset.xhtml?persistentId=, doi: 10.5683/SP/MBMQGD.

[43] H. Trabelsi, I. Zghal, and N. Slokom, "Segmentation of cyctoids macular edema in optical cohenrence tomography," in *Proc. 2nd Int. Conf. Adv. Technol. Signal Image Process. (ATSIP)*, Mar. 2016, pp. 303–306.

[44] S. S. Al-Amri, N. V. Kalyankar, and S. D. Khamitkar, "Image segmentation by using threshold techniques," 2010, *arXiv:1005.4020*. [Online]. Available: http://arxiv.org/abs/1005.4020

[45] H.-J. He, C. Zheng, and D.-W. Sun, "Image segmentation techniques," in *Computer Vision Technology for Food Quality Evaluation*. New York, NY, USA: Academic, 2016, pp. 45–63.

[46] R. C. Gonzalez, R. E. Woods, and S. L. Eddins, *Digital Image Processing Using MATLAB*. London, U.K.: Pearson, 2004.

[47] S. Suzuki and K. Be, "Topological structural analysis of digitized binary images by border following," *Comput. Vis., Graph., Image Process.*, vol. 30, no. 1, pp. 32–46, Apr. 1985.

[48] (2019). *Metrics to Evaluate Your Semantic Segmentation Model Towards Data Science*. Accessed: Apr. 14, 2020. [Online]. Available: https://towardsdatascience.com/metrics-to-evaluate-your-semantic-segmentation-model-6bcb99639aa2

[49] S. Kusuhara, "Prediction of postoperative visual outcome based on hole configuration by optical coherence tomography in eyes with idiopathic macular holes," *Amer. J. Ophthalmol.*, vol. 138, no. 5, pp. 709–716, 2004.

[50] B. Haouchine, P. Massin, R. Tadayoni, A. Erginay, and A. Gaudric, "Diagnosis of macular pseudoholes and lamellar macular holes by optical coherence tomography," *Amer. J. Ophthalmol.*, vol. 138, no. 5, pp. 732–739, Nov. 2004.

[51] R. Y. Foos and N. C. Wheeler, "Vitreoretinal juncture: Synchysis senilis and posterior vitreous detachment," *Ophthalmology*, vol. 89, no. 12, pp. 1502–1512, 1982.
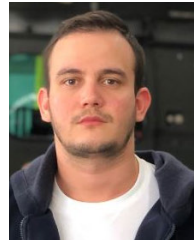
ODILON L. C. MENDES received the B.Eng. degree in mechatronics engineering and the M.Eng. degree in telecommunications engineering with sandwich graduation from Arizona State University, USA, and the Instituto Federal do Ceará (IFCE), Fortaleza, Brazil, in 2018 and 2020, respectively. He is currently pursuing the M.Sc. degree in aviation safety and continued airworthiness with the Instituto Tecnológico de Aeronáutica (ITA). He is currently pursuing the Ph.D. degree in electrical engineering with the Universidade Federal do Ceará (UFC). As a researcher, he works in the fields of robotics, control systems, computer vision, biomedical engineering, and aviation safety.

DANIEL R. LUCENA received the Ph.D. degree in ophthalmology from the Faculty of Medicine of Ribeirão Preto, Universidade de São Paulo (USP), Brazil, in 2004. He was a Fellow in ocular ultrasound from the Retina and Vitreous from Advanced Retina and Cataract Center (CARC), Brazil, in 1999. From 2000 to 2001, he was a Fellow in retina and vitreous from the Retina and Vitreous Specialized Center (CERV), Brazil. He was a Fellow in cornea and laser refractive surgery, in 2001. He was a Fellow in uveitis with the Universidade Federal de Minas Gerais (UFMG), Brazil, in 2001. He is currently the Chief of the Retina Sector of the Escola Cearense de Oftalmologia and the Santa Casa de Misericórdia, Fortaleza, Brazil. He was a Scientific Reviewer of the journals: *International Journal of Retina and Vitreous*, *Graefe's Archive for Clinical and Experimental Ophthalmology*, and *Arquivos Brasileiros de Oftalmologia*.

ABRAHÃO R. LUCENA graduated in medicine from the Universidade de Federal da Paraíba, in 1998. He received the M.Sc. and Ph.D. degrees in ophthalmology from the Faculty of Medicine of Ribeirão Preto, Universidade de São Paulo (USP), Brazil, in 2004 and 2008, respectively. He has specialization in ophthalmology with the Altino Ventura Foundation/Pernambuco Eye Hospital, in 2000. He was a Fellow in cornea and laser refractive surgery, in 2001. He is currently a Coordinator of the Escola Cearense de Oftalmologia, cataract sector of the Center of Ophthalmology. He was the President of the Cearense Society of Ophthalmology from 2016 to 2018, the President of the Cooperative of Ophthalmologists of the State of Ceará from 2012 to 2014 and from 2014 to 2016, the Vice President of the Cearense Society of Ophthalmology from 2014 to 2016, the Co-Editor of the *Brazilian Journal of Ophthalmology* from 2012 to 2014, an Elected Councilor of the Council of Guidelines and Management of the Brazilian Council of Ophthalmology from 2015 to 2017, the first Secretary of the Brazilian Council of Ophthalmology from 2017 to 2019, a Fiscal Holder Councilor of the Brazilian Council of Ophthalmology from 2019 to 2021, and the Chief Editor of *North-Northeast Journal of Ophthalmology*.

TARIQUE S. CAVALCANTE received the M.Eng. and Ph.D. degrees in teleinformatics engineering from the Universidade Federal do Ceará (UFC), Brazil, in 2010 and 2016, respectively. He has specialization in project management with the Universidade de Fortaleza (UNIFOR), Brazil, in 2012. He graduated in industrial mechatronics from the Instituto Federal do Ceará (IFCE), Fortaleza, in 2008. He is currently a Professor with the IFCE, in the area of automation and control of industrial processes. He is also the Chief of the Department of Innovation of the Dean of Research, Graduate Studies and Innovation, IFCE, in addition to being part of the Faculty of the Graduate Programs in Telecommunications Engineering, IFCE. As a researcher, he works in the fields of computer vision, artificial intelligence, biomedical engineering, cognitive computing and industrial automation, coordinating and guiding several projects at a technical and higher level. He works in the management of the Fortaleza Innovation Pole (EMBRAPII), in addition to developing P, D&I projects for the productive sector.

VICTOR HUGO C. DE ALBUQUERQUE (Senior Member, IEEE) graduated in mechatronics engineering from the Federal Center of Technological Education of Ceará (CEFETCE), in 2006. He received the M.Sc. degree in teleinformatics engineering from the Federal University of Ceará (UFC), in 2007, and the Ph.D. degree in mechanical engineering from the Federal University of Paraíba (UFPB), in 2010. He is currently a collaborator Professor and a Senior Researcher with the Graduate Program on Teleinformatics Engineering, Federal University of Ceará, Brazil, and the Graduate Program on Telecommunication Engineering, Federal Institute of Education, Science and Technology of Ceará, Fortaleza, Brazil. He is a Specialist, mainly, in image data science, the IoT, machine/deep learning, pattern recognition, and robotic.

METEB ALTAF received the Ph.D. degree from Brunel University London, London, U.K., in 2009. Since then, he joined KACST as an Assistant Research Professor. He was appointed as the Director Assistant of Administrative Affairs and Scientific Affairs at the National Center for Robotics and Intelligent Systems. After that, he was appointed as the Director of the National Robotics Technology and Intelligent Systems Center before it became known as the National Center for Robotics Technology and Internet of Things. He was then promoted to Research Associate Professor. In the meantime, he became the Director of the Innovation Center for Industry 4.0, King Abdulaziz City for Science and Technology. He is currently the Director of Advanced Manufacturing and Industry 4.0 Center. He is also lecturing at the Biomedical Technology Department, King Saud University. During his career, he has published a number of papers in different well-known ISI journals and in well recognized conferences. He has supervised more than 20 research projects locally and internationally as technology transfer projects.

MOHAMMAD MEHEDI HASSAN (Senior Member, IEEE) received the Ph.D. degree in computer engineering from Kyung Hee University, South Korea, in February 2011. He is currently a Professor with the Information Systems Department, College of Computer and Information Sciences (CCIS), King Saud University (KSU), Riyadh, Saudi Arabia. He has authored or coauthored more than 260+ publications, including refereed journals (218+ SCI/ISI-indexed journal articles, four+ ESI highly cited articles, and one hot article), conference papers, books, and book chapters. His research interests include cloud/edge computing, the Internet of Things, artificial intelligence, body sensor networks, big data, mobile computing, cyber security, smart computing, 5G/6G networks, and social networks. He was a recipient of a number of awards, including the Distinguished Research Award from College of Computer and Information Sciences, the KSU 2020, the Best Conference Paper Award from IEEE International Conference on Sustainable Technologies for Industry 4.0 (STI) 2020, the Best Journal Paper Award from IEEE Systems Journal, in 2018, the Best Conference Paper Award from CloudComp in 2014 conference, and the Excellence in Research Award from College of Computer and Information Sciences, KSU, in 2015 and 2016. He is listed as one of the top 2% scientists of the world in networking and telecommunication field. He is one of the top computer scientists in Saudi Arabia as well. He is on the editorial board of several SCI/ISI-indexed journals. He has also played role of the guest editor of several international ISI-indexed journals.

AUZUIR R. ALEXANDRIA graduated in electrical engineering and in computer science from the Universidade Federal de Campina Grande (UFCG), Brazil, in 1993 and 1994, respectively. He received the M.Sc. and Ph.D. degrees in teleinformatics engineering from the Universidade Federal do Ceará (UFC), Brazil, in 2005 and 2011, respectively. Since 2003, he has been a Professor with the Department of Industry, Instituto Federal do Ceará (IFCE), Fortaleza. From 1993 to 2005, he worked for local companies, in the industrial, and hardware and software development areas. He participated of the preparation of the mechatronics engineering course where he served as a coordinator. He participates as a Permanent Professor with the Postgraduate Programs in Telecommunications Engineering and Renewable Energies. As a researcher, he works in the fields of computer vision, mobile robotics, biomedical engineering, artificial neural networks and industrial automation, coordinating and guiding several projects at a technical and higher level. He is the leader of the computational simulation and robotics research groups.

● ● ●